

FULL PAPER

Open Access



# Hollow Ni/NiO/C composite derived from metal-organic frameworks as a high-efficiency electrocatalyst for the hydrogen evolution reaction

Ha Huu Do<sup>1</sup>, Mahider Asmare Tekalgne<sup>1</sup>, Quyet Van Le<sup>2</sup>, Jin Hyuk Cho<sup>2</sup>, Sang Hyun Ahn<sup>1\*</sup> and Soo Young Kim<sup>2\*</sup> 

## Abstract

Metal-organic frameworks (MOFs) constitute a class of crystalline porous materials employed in storage and energy conversion applications. MOFs possess characteristics that render them ideal in the preparation of electrocatalysts, and exhibit excellent performance for the hydrogen evolution reaction (HER). Herein, H-Ni/NiO/C catalysts were synthesized from a Ni-based MOF hollow structure via a two-step process involving carbonization and oxidation. Interestingly, the performance of the H-Ni/NiO/C catalyst was superior to those of H-Ni/C, H-NiO/C, and NH-Ni/NiO/C catalysts for the HER. Notably, H-Ni/NiO/C exhibited the best electrocatalytic activity for the HER, with a low overpotential of 87 mV for 10 mA cm<sup>-2</sup> and a Tafel slope of 91.7 mV dec<sup>-1</sup>. The high performance is ascribed to the synergistic effect of the metal/metal oxide and hollow architecture, which is favorable for breaking the H-OH bond, forming hydrogen atoms, and enabling charge transport. These results indicate that the employed approach is promising for fabricating cost-effective catalysts for hydrogen production in alkaline media.

**Keywords** MOFs, Ni/NiO/C, Hollow structure, Electrocatalyst, HER

## 1 Introduction

The discovery of green energy sources has contributed significantly to the implementation of sustainable development practices in society, necessitated by the rising concerns associated with the negative impacts of fossil fuels on the environment. Hydrogen (H<sub>2</sub>) has been evaluated as a potential replacement for fossil fuels

owing to its energy efficiency and eco-friendly properties [1–5]. Among the available methods for hydrogen production, water splitting exhibits promise. Typically, Pt-based materials exhibit excellent catalytic activity for water dissociation [6–8]. However, their lack of stability and high cost hinder their utilization on an industrial scale. Accordingly, numerous studies have explored the use of non-noble metal catalysts, such as transition metal selenides [9–11], metal nitrides [12–14], and metal carbides [15–17], which exhibit promising activity in acidic solutions [18–22]. However, their performance is still limited for the hydrogen evolution reaction (HER) in alkaline environments. This is because extra energy must be supplied for the Volmer process. To address this issue, many studies related to the use of Ni/NiO-based electrocatalysts for the HER under alkaline conditions have been conducted. Because Ni metal has relatively

\*Correspondence:

Sang Hyun Ahn  
shahn@cau.ac.kr

Soo Young Kim  
sooyoungkim@korea.ac.kr

<sup>1</sup> School of Chemical Engineering and Materials Science, Chung-Ang University, 84 Heukseok-Ro, Dongjak-Gu, Seoul 06974, Republic of Korea

<sup>2</sup> Department of Materials Science and Engineering, Institute of Green Manufacturing Technology, Korea University, 145 Anam-Ro, Seongbuk-Gu, Seoul 02841, Republic of Korea



© The Author(s) 2023. **Open Access** This article is licensed under a Creative Commons Attribution 4.0 International License, which permits use, sharing, adaptation, distribution and reproduction in any medium or format, as long as you give appropriate credit to the original author(s) and the source, provide a link to the Creative Commons licence, and indicate if changes were made. The images or other third party material in this article are included in the article's Creative Commons licence, unless indicated otherwise in a credit line to the material. If material is not included in the article's Creative Commons licence and your intended use is not permitted by statutory regulation or exceeds the permitted use, you will need to obtain permission directly from the copyright holder. To view a copy of this licence, visit <http://creativecommons.org/licenses/by/4.0/>.

appropriate Gibbs free energy of adsorbed atomic hydrogen ( $-0.27$  eV) for HER [23]. Moreover, Ni is a non-noble metal, implying the synthesis of low-cost electrocatalysts from Ni-based materials [24]. On the other hand, NiO is effective for the dissociation of water molecules due to its defects [25]. For example, Oshchepkov et al. demonstrated the role of NiO in enhancing the HER performance of a Ni catalyst [26]. Yan et al. created a core-shell Ni/NiO architecture with outstanding durability [27]. Wang et al. recognized that the use of an appropriate Ni/NiO ratio results in a low overvoltage [28]. Yang et al. deposited carbon nanotubes on Ni/NiO nanofibers to achieve a high HER efficiency with a low overvoltage [29]. Overall, metal oxides play a vital role in the Volmer step, leading to improved HER activity [30–34]. They act as absorbents and scavenge hydroxyl ions, blocking the active metal sites.

Hollow-structured materials have also been considered as potential electrocatalysts for the HER. Hollow structures possess thin shells with inner and outer surfaces to afford a larger surface area and more exposed active sites that promote reactant adsorption and redox reactions, providing these surfaces with locally incompatible cofactors for oxidative and reductive reactions [35, 36]. In addition, hollow structures allow a shortened path for charge transport during the catalytic process and facilitate the growth of the other active materials [37–39]. For example, Nguyen et al. found that  $WS_2$  hollow spheres exhibited a higher HER catalytic activity than  $WS_2$  with a non-hollow structure [40]. Ganesan and Kim designed  $CoS_2$ - $MoS_2$  with a hollow architecture as a high-efficiency catalyst for the HER [41]. The effectiveness of the hollow structure was reported by Xia [42], who highlighted that  $CoP@MoS_2$  hollow nanocatalysts with a small Tafel slope are promising for the HER. Furthermore, Metal-organic frameworks (MOFs) are ideal for the synthesis of hollow-structured catalysts because of the level of morphological control they provide via changing the linkers and reaction conditions. In addition, MOFs possess a high porosity, which increases the active site density. Xue et al. employed ZIF-67 as a template to prepare  $CoSe_2$ - $FeSe_2$  catalysts with a hollow architecture for the HER under alkaline conditions [43]. Tian et al. used a Ni-MOF to create  $NiS_2$  hollow microspheres as highly stable catalysts for the HER [44]. As mentioned above, the use of Ni/NiO with a hollow structure derived from the MOF may lead to remarkable HER performance.

In this study, we used a Ni-MOF hollow structure to prepare a Ni/NiO/C hollow-structured composite through the two-step route of carbonization and oxidation. This material showed enhanced HER activity compared with Ni/C, NiO/C, and Ni/NiO/C with a non-hollow structure. Moreover, it exhibited

a very low overpotential of 87 mV at a current density of  $10 \text{ mA cm}^{-2}$  and good durability. The approach employed herein could serve as a novel route for the synthesis of hollow-structured catalysts for the HER and other applications.

## 2 Materials and methods

### 2.1 Chemicals and materials

Nickel nitrate hexahydrate ( $Ni(NO_3)_2 \cdot 6H_2O$ ), benzene-1,3,5-tricarboxylic acid ( $H_3BTC$ , 95%), N, N-dimethylformamide (DMF), and polyvinylpyrrolidone (PVP,  $M_w=40,000$ ) and ethanol ( $C_2H_5OH$ ) were purchased from Sigma Aldrich. Deionized water (DI) was prepared using a Millipore Milli-Q apparatus.

### 2.2 Fabrication of the Ni-MOF hollow structure

Typically, a Ni-MOF hollow structure was synthesized according to a reported study with a slight modification [45].  $Ni(NO_3)_2 \cdot 6H_2O$  (216 mg) and  $H_3BTC$  (75 mg) were dissolved in a mixed solvent containing 5 mL of DMF, 5 mL of  $C_2H_5OH$ , and 5 mL of DI for 30 min under magnetic stirring. Subsequently, 750 mg of PVP, which acted as a micelle stabilizer, was added to this mixture under magnetic stirring for 2 h to form a homogeneous solution. This solution was transferred into a 25 mL Teflon-lined stainless-steel reactor and heated to  $150^\circ\text{C}$  for 10 h. The obtained light-green Ni-MOF crystals were washed by  $C_2H_5OH$  and dried at  $60^\circ\text{C}$  for 10 h.

### 2.3 Fabrication of hollow-structured composites

The Ni-MOF powders were placed into an alumina crucible and heated at  $450^\circ\text{C}$  for 2 h under a  $N_2$  gas to form the hollow architecture of H-Ni/C. Subsequently, this powder was oxidized in air at  $250^\circ\text{C}$  for 20 min to obtain the H-Ni/NiO/C composite. H-NiO/C was obtained by heating the Ni-MOF hollow structure at  $450^\circ\text{C}$  for 2 h. In addition, a non-hollow structure of NH-Ni/NiO/C was fabricated from a Ni-MOF non-hollow structure in the same manner as for the synthesis of the H-Ni/NiO/C composite.

### 2.4 Material characterization

The morphological structure of the as-synthesized products was confirmed using scanning electron microscopy (SEM, Carl Zeiss) and transmission electron microscopy (TEM, JEOL). X-ray diffraction (XRD) tests were performed with a Bruker D8-Advance diffractometer. Raman curves of the composites were tested on a LabRAM-HR Evolution spectrometer with a 532 nm laser. The elemental composition was determined using X-ray photoelectron spectroscopy (XPS, K-alpha).

## 2.5 Electrochemical measurements

The HER performance was evaluated using various electrochemical techniques with the help of an Ivium 55,630 instrument. The electrochemical system contained a graphite rod as the counter electrode, Hg/HgO electrode as the reference electrode, and 1 M KOH as the electrolyte. The working electrode was fabricated as follows: the as-synthesized materials (30 mg) were sonicated in a mixture containing 0.1 mL Nafion (5 wt%) and 3 mL C<sub>2</sub>H<sub>5</sub>OH for 30 min. Subsequently, a certain volume of the homogeneous suspension was coated on the surface of a glassy carbon electrode (diameter of 3 mm), with a catalyst loading of 0.30 mg cm<sup>-2</sup>. Polarization curves were collected with IR correction at a scan rate of 2 mV s<sup>-1</sup>. IR corrections for resistance were conducted using electrochemical impedance spectroscopy (EIS) in the potentiostatic mode from 100,000 to 0.1 Hz. Cyclic voltammetry (CV) was performed to determine

the electrochemical double-layer capacitance ( $C_{dl}$ ) in the non-faradaic voltage region at 20, 40, 60, 80, 120, and 140 mV s<sup>-1</sup>. The reported potentials were converted to those of the reversible hydrogen electrode (RHE) using the following relation:  $E_{RHE} = E_{Hg/HgO} + 0.098 + 0.059pH$ .

## 3 Results and discussion

Herein, we used a Ni-MOF hollow structure to fabricate H-Ni/NiO/C via a two-step process involving pyrolysis and oxidation, as schematically shown in Fig. 1. The Ni-MOF hollow precursor was synthesized through a typical synthetic route [46, 47]. Subsequently, the as-synthesized Ni-MOF hollow precursor was carbonization for 2 h to prepare H-Ni/C, followed by oxidation in the air for various durations to form H-Ni/NiO/C. In this step, the Ni species that were embedded in the carbon skeleton partially oxidized into NiO phases. Moreover, H-NiO/C was

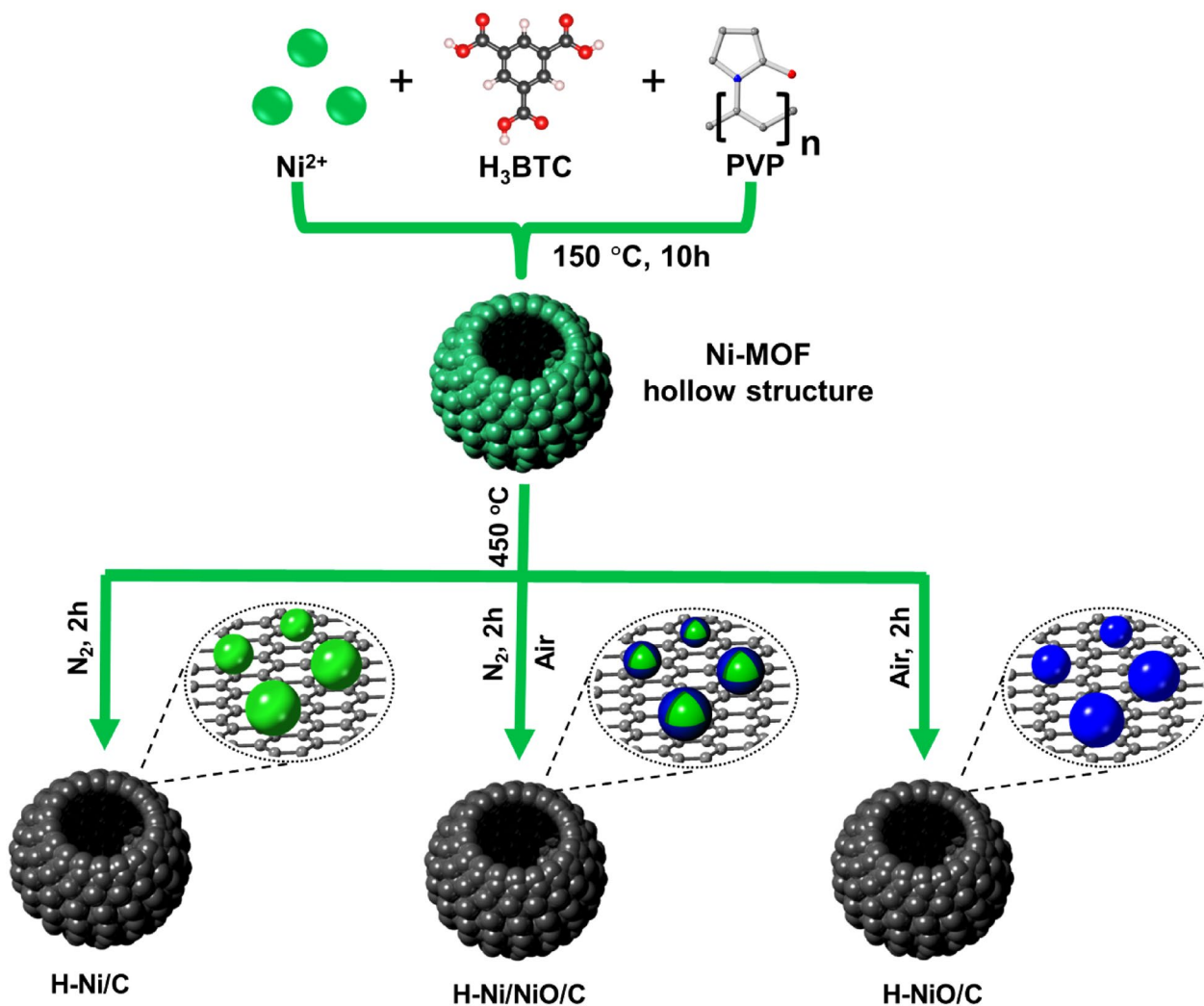


**Fig. 1** Schematic illustrating the fabrication of H-Ni/C, H-Ni/NiO/C, and H-NiO/C catalysts

generated by the direct calcination of the Ni-MOF precursor at 450 °C in the air for 2 h. The phase structures and microtopographies of the Ni-MOF and its derivatives were analyzed using XRD and SEM. The XRD patterns in Additional file 1: Fig. S1a show a main peak at 13.0° ascribed to the Ni-MOF, indicating the existence of an organic composition [45, 47–49]. The Ni-MOF crystals exhibit a spherical morphology with an average size of 1.5 μm. The hollow structure of the Ni-MOF was confirmed by SEM (Additional file 1: Fig. S1b). The surface of the microspheres was not smooth, implying that they were assembled from nanoparticles. As depicted in the SEM images (Fig. 2a and Additional file 1: Fig. S2), the H–Ni/C, H–Ni/NiO/C, and H–NiO/C spheres possess a well-preserved hollow architecture similar to that of the hollow Ni-MOF precursor. This indicates that the carbon skeleton does not collapse during pyrolysis and oxidation. In addition, the SEM image in Fig. 2b confirms the synthesis of Ni/NiO/C with a non-hollow structure and an average size of 0.5 × 3 μm. The TEM image (Fig. 2c) verifies that the H–Ni/NiO/C samples possess a hollow morphological structure with a particle diameter of 1.4 μm. The high-resolution TEM image indicates that the Ni/NiO nanograins are embedded in the carbon matrix (Fig. 2d). The d-spacing of 0.178 nm was indexed to the (200) crystal plane of metallic Ni, whereas that of 0.209 nm is assigned to the (200) crystal plane of the NiO phase. Moreover, (111) crystal plane of H–Ni/C with a d-spacing of 0.202 nm is indicated in Additional file 1: Fig. S3. As depicted in Fig. 2e–h, scanning TEM and a

corresponding elemental mapping of H–Ni/NiO/C indicate the well-distribution of elements (Ni, O, C).

Figure 3a shows the XRD patterns of H–Ni/C, H–Ni/NiO/C, and H–NiO/C. The peaks at 2θ values of 44.3°, 51.5°, and 76.1° can be indexed to the (111), (200), and (220) planes of metallic Ni (PDF 00-001-1258), respectively. The XRD pattern of H–NiO/C shows peaks at 37.2°, 43.2°, and 62.9°, which are assigned to the (111), (200), and (220) planes (PDF 00-004-0835), respectively [50, 51]. The Raman spectra of the H–Ni/C, H–Ni/NiO/C, and H–NiO/C catalysts are shown in Fig. 3b. The H–Ni/C sample is not Raman-active because there is no observable change in the polarizability of metallic Ni [52]. The spectrum for H–NiO/C displays five peaks at 360, 510, 680, 840, and 1060 cm<sup>-1</sup>, whereas that for H–Ni/NiO/C exhibits two peaks at 500 and 1060 cm<sup>-1</sup>. The Raman peaks at 360 and 500–510 cm<sup>-1</sup> can be indexed to the one-phonon (1P) transverse optical (TO) and longitudinal optical (LO) vibrations of the Ni–O bonds. The other peaks are assigned to the second-order vibrational modes of 2P<sub>TO</sub>, 2P<sub>TO+LO</sub>, and 2P<sub>LO</sub>, respectively [53, 54]. Interestingly, the intensity of 1P<sub>LO</sub> increased, whereas the intensity of 2P<sub>LO</sub> decreased in the H–Ni/NiO/C. Because the intensity of 1P<sub>LO</sub> and 2P<sub>LO</sub> was related to the defect states associated with Ni vacancies [55, 56]. According to Mishra et al., the increased temperature reduces the Ni vacancies [57], which dominates the intensity of 1P<sub>LO</sub> [58]. Therefore, the high intensity of 1P<sub>LO</sub> could be ascribed to a large number of Ni vacancies in H–Ni/NiO/C, which was formed at 250 °C. H–NiO/C created

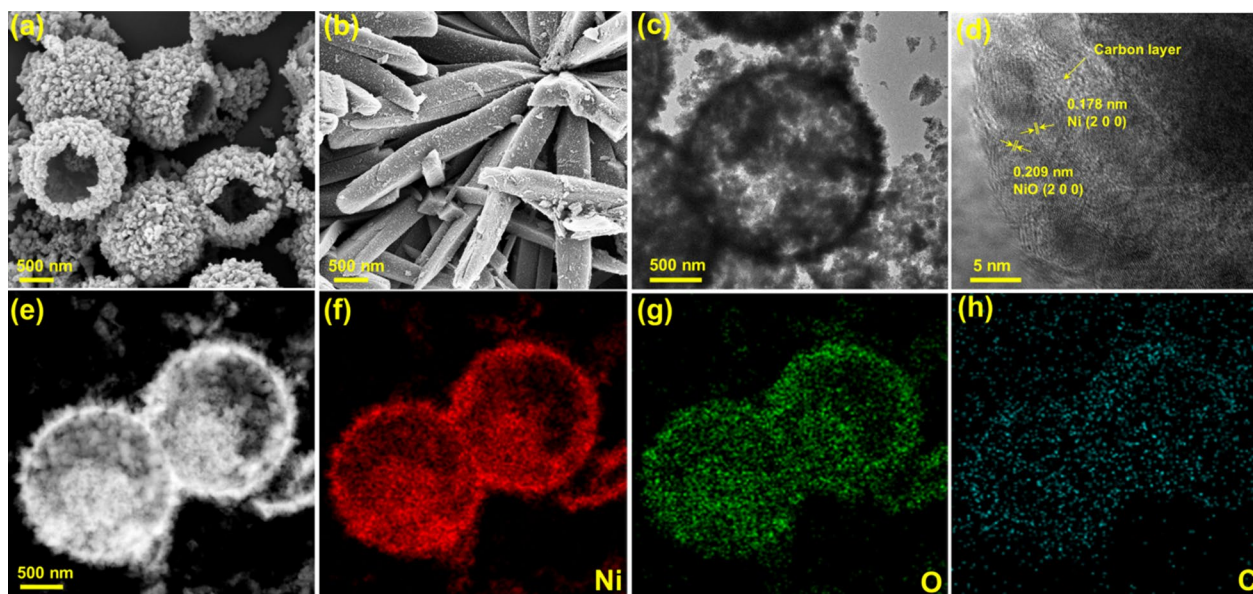


**Fig. 2** SEM images of **a** H–Ni/NiO/C and **b** H–NiO/C, **c** TEM, **d** HR-TEM, **e** Scanning TEM images of H–Ni/NiO/C with corresponding element maps of **f** Ni, **g** O, and **h** C

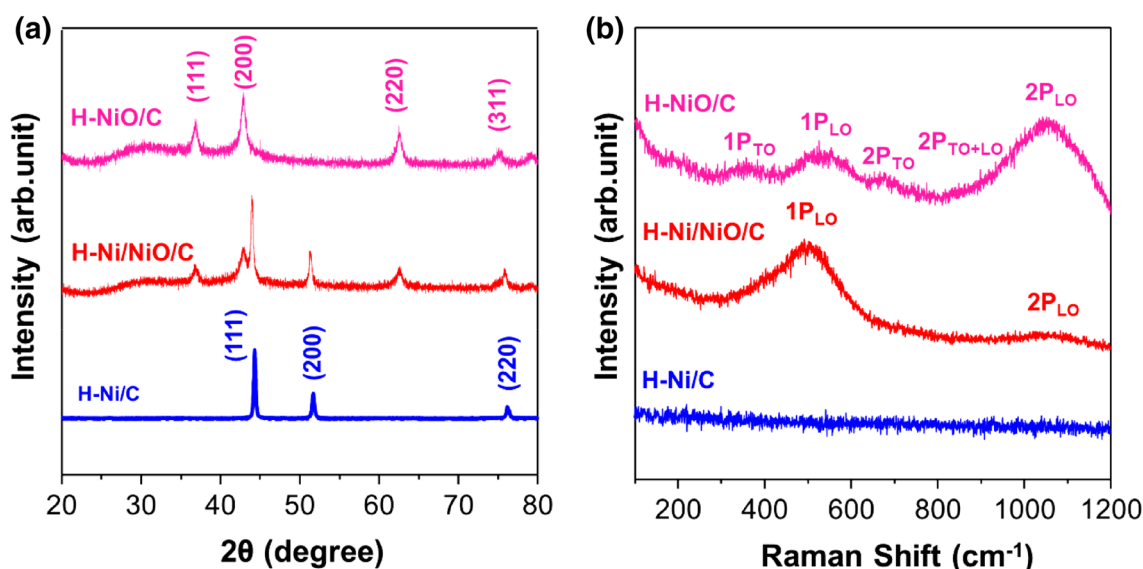


**Fig. 3** **a** XRD patterns and **b** Raman spectrum of H-Ni/C, H-Ni/NiO/C, and H-NiO/C

at 450 °C shows a low intensity of  $1P_{LO}$  mode, which was attributed to the decelerated Ni vacancies. Also, the intensity of  $2P_{LO}$  was accelerated due to the improved crystalline quality of the H-NiO/C sample [59].

The valence states of Ni, C, O were confirmed by XPS. Peaks of these elementals are clearly observed in the total XPS profiles of H-Ni/NiO/C in Fig. 4a. Notably, the HR XPS profiles of Ni 2p are deconvoluted into two main peaks,  $Ni^{2+} 2p_{1/2}$  and  $Ni^{2+} 2p_{3/2}$ , as depicted in Fig. 4b. Notably, a multiplet-split  $Ni^{2+} 2p_{3/2}$  at 853.7 and 855.5 eV, and a  $Ni^{2+} 2p_{3/2}$  satellite at 860.8 eV. Also, the peaks at 870.9 eV and 872.4 eV correspond to the multiplet-split  $Ni^{2+} 2p_{1/2}$  and  $Ni^{2+} 2p_{3/2}$  of NiO phases, respectively [27]. This is also confirmed in the XPS spectrum of Ni 2p for the H-NiO/C sample (Additional file 1: Fig. S4). More importantly, Peaks at 852.6 eV for metallic Ni  $2p_{3/2}$  and 869.9 eV for metallic Ni  $2p_{1/2}$  (Additional file 1: Fig. S5) do not appear in the XPS spectrum of H-Ni/NiO/C sample, whereas XRD patterns confirmed metallic Ni in H-Ni/NiO/C [51]. This outcome was attributed to the formation of NiO on the surface metallic Ni and the difference in depth penetration in the sample of the two methodologies [60]. Figure 4c shows the O1s spectra of H-Ni/NiO/C; the two characteristic peaks are attributed to Ni-O (529.3 eV) and -OH/oxygen vacancies (531.1 eV) [27]. The C1s spectra of H-Ni/NiO/C exhibit three types of contributions. The peaks at binding energies of 284.7, 285.4, and 288.4 eV can be indexed to the C-C, C-OH, and O-C=O bonds, respectively [61]. Besides, the Ni:O:C atomic ratio measured from XPS is equal to 34.76:43.72:21.52. Ni concentration (34.76%) is smaller than the concentration of oxygen (43.72%), which

implies the high Ni vacancies in the H-Ni/NiO sample. This is consistent with the Raman spectra of the H-Ni/NiO/C sample. Rich Ni vacancies in H-Ni/NiO/C can illustrate abundant active centers for HER [58].

The HER performances of H-Ni/C, H-Ni/NiO/C, H-NiO, and NH-Ni/NiO/C were investigated in a 1.0 M potassium hydroxide medium. As displayed in Fig. 5a, H-Ni/NiO/C exhibits a higher catalytic activity than H-Ni/C, H-NiO, and NH-Ni/NiO/C (Additional file 1: Fig. S6). To achieve an HER current density of  $10 \text{ mA cm}^{-2}$ , the H-Ni/C, H-Ni/NiO/C, H-NiO, and NH-Ni/NiO/C electrocatalysts require overpotentials of 167, 87, 246, and 117 mV, respectively (Additional file 1: Table S1). A lower overvoltage indicates a lower energy barrier requirement for the HER. During the HER with the H-Ni/NiO/C electrocatalyst, the NiO species plays an important role in breaking the H-OH bond to generate H atoms, which then traverse to the Ni species before forming  $H_2$  molecules [23, 25, 62, 63]. When using the H-Ni/C electrocatalyst, the active sites are impeded by the OH<sup>-</sup> ions generated from water dissociation [52, 64]. Moreover, the hollow materials provide more exposed active centers than their bulk counterparts and enable electron transfer during the catalytic process [42, 65, 66]. Therefore, the hollow structure of H-Ni/NiO/C exhibits a higher HER activity than that of the non-hollow structure of NH-Ni/NiO/C. Also, H-Ni/NiO/C originated from Ni-MOF hollow structure exhibits a lower overpotential than the other electrocatalysts, which were not synthesized from MOFs precursors (Additional file 1: Table S2). Furthermore, using MOFs can easily control the morphology of electrocatalysts by changing reaction conditions. This outcome proved the advantage of

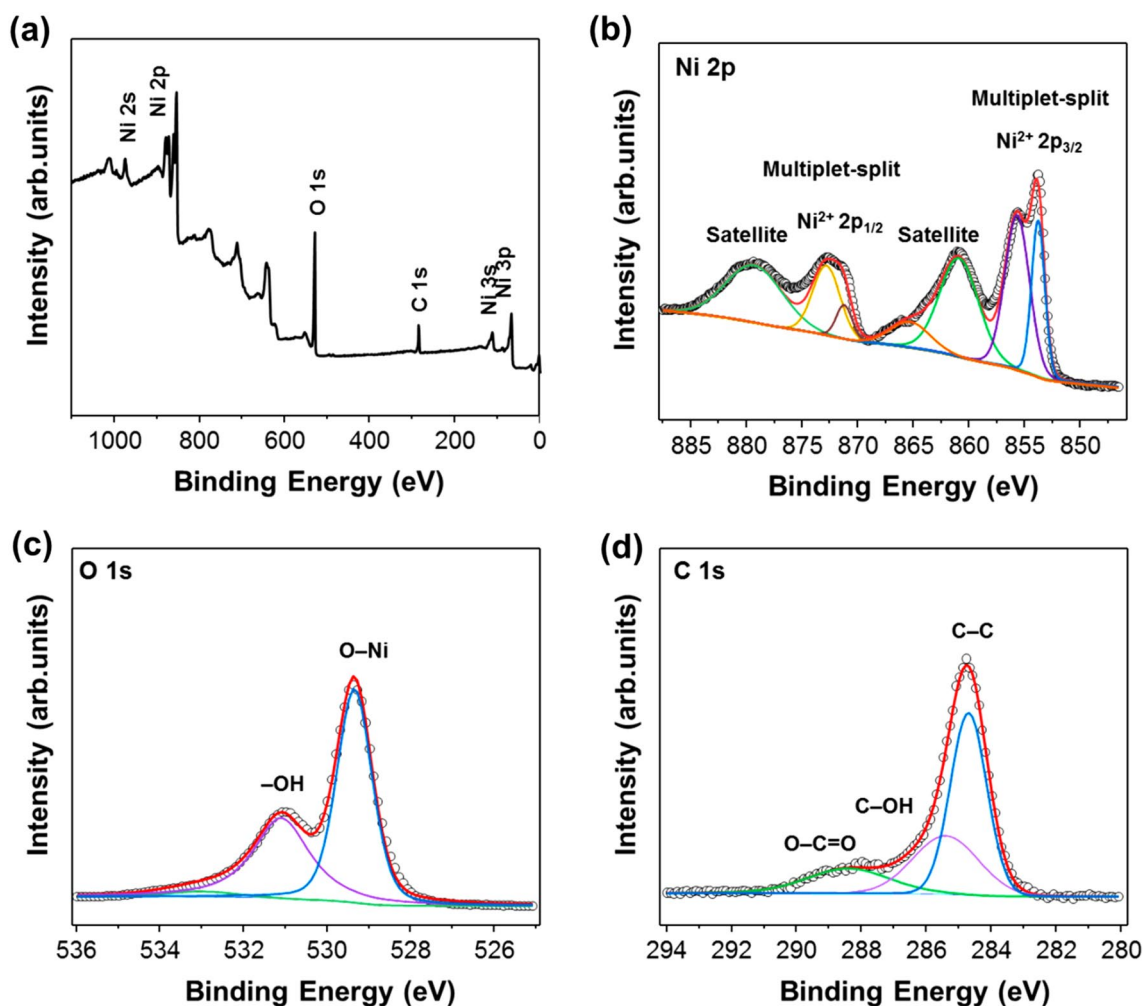
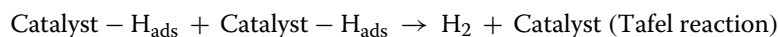
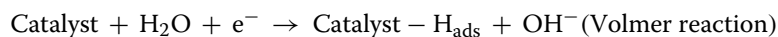


**Fig. 4** a XPS survey spectrum. High-resolution XPS profiles of H-Ni/NiO/C: **b** Ni 2p, **c** O 1s, and **d** C 1s

MOFs for the preparation of electrocatalysts for HER. In addition, the Tafel plots show that the HER performance of H-Ni/NiO/C is superior to those of the other catalysts (Fig. 5b). In particular, the Tafel slopes of H-Ni/C, H-Ni/NiO/C, H-NiO, and NH-Ni/NiO/C are 106.5, 91.7, 124.2, and 98.7  $\text{mV dec}^{-1}$ , respectively. Typically, the HER in an alkaline solution involves three basic reactions, as follows:



In the Volmer reaction (Tafel slope  $\approx 120 \text{ mV dec}^{-1}$ ), the H-OH bond breaks to form H atoms that are absorbed

on the surface of the catalyst. The Heyrovsky reaction (Tafel slope  $\approx 40 \text{ mV dec}^{-1}$ ) describes electrochemical desorption, whereas the Tafel reaction (Tafel slope  $\approx 30 \text{ mV dec}^{-1}$ ) expresses chemical desorption to form hydrogen. Based on the reported Tafel slopes, the Volmer and Heyrovsky reactions occur when using the investigated catalysts.

EIS was performed on the catalysts to confirm the reaction kinetics of the electrodes. Figure 5c shows

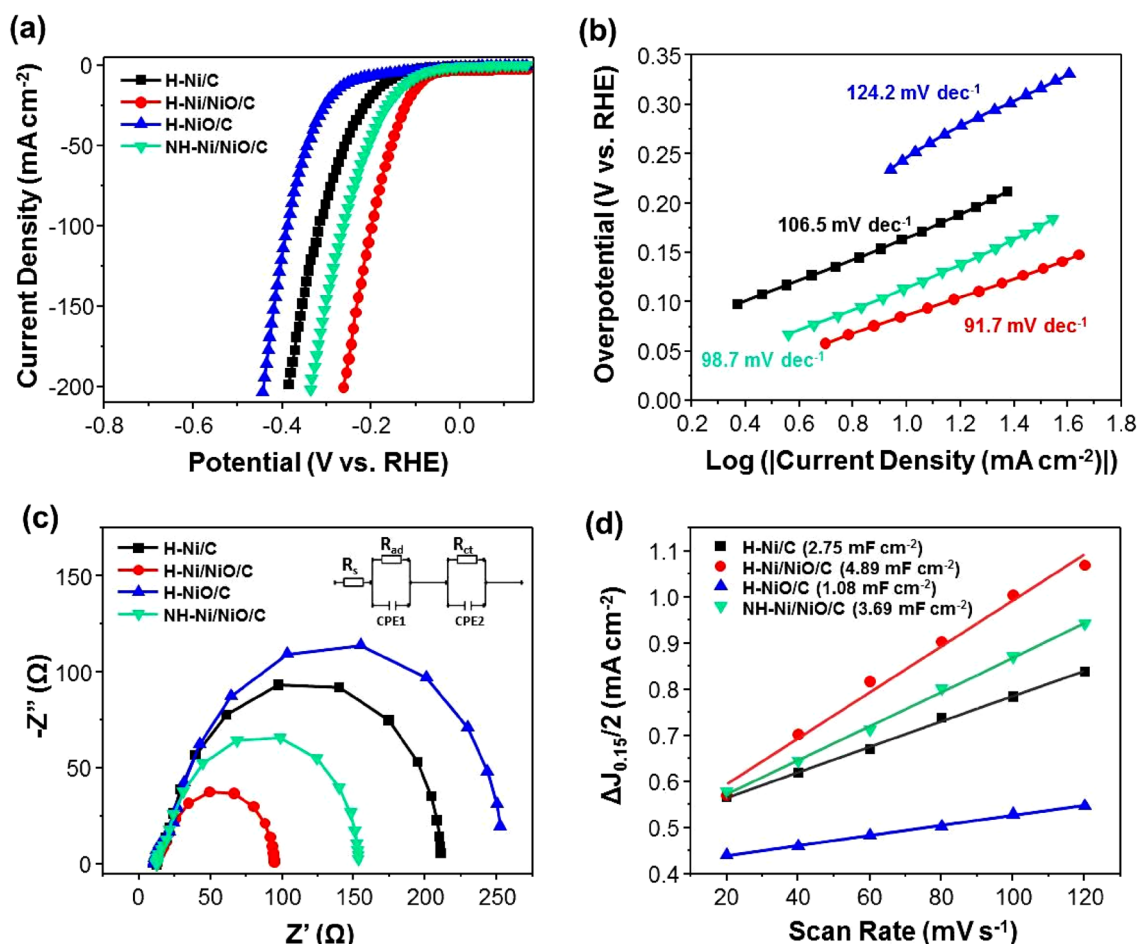


**Fig. 5** **a** Polarization curve of H-Ni/C, H-Ni/NiO/C, H-NiO/C, and NH-Ni/NiO/C. **b** Tafel slope of catalysts, **c** Nyquist plots of different samples recorded at a potential of  $-0.2$  V vs. the RHE. **d** Double-layer capacitances of various samples obtained using CV

the Nyquist plots of the four samples, which are fitted with an equivalent circle (inset of Fig. 5c) to determine the charge transfer resistance ( $R_{ct}$ ). Note that the  $R_{ct}$  of H-Ni/NiO/C is 75  $\Omega$ , which is much lower than that of H-Ni/C (189  $\Omega$ ), H-NiO (229.4  $\Omega$ ), and NH-Ni/NiO/C (133.4  $\Omega$ ). The lowest  $R_{ct}$  of H-Ni/NiO/C is indicative of the fastest interfacial charge transport kinetics of this catalyst during the electrocatalytic process. Typically, the electrochemical surface area (ECSA) can be predicted from  $C_{dl}$ , which is derived from the CV profiles in the non-faradaic potential region. The CV profiles of H-Ni/C (Additional file 1: Fig. S7a), H-Ni/NiO/C (Additional file 1: Fig. S7b), H-NiO (Additional file 1: Fig. S7c), and NH-Ni/NiO/C (Additional file 1: Fig. S7d) were acquired in the potential window of 0.1 to 0.2 V (vs. the RHE) at various scan rates. The slope of the plot of  $\Delta J/2$  at 0.15 V (vs the RHE) versus the scan rate is  $C_{dl}$ . The  $C_{dl}$  of H-Ni/NiO/C is 4.89 mF cm<sup>-2</sup>, which is larger than those of H-Ni/C (2.75 mF cm<sup>-2</sup>), H-NiO (1.08 mF cm<sup>-2</sup>), and NH-Ni/NiO/C

(3.69 mF cm<sup>-2</sup>), implying its larger ECSA as well as superior HER performance (Fig. 5d). The durability of H-Ni/NiO/C was evaluated using the CV profiles and the constant potential method. The results are shown in Fig. 6a. The linear sweep voltammetry (LSV) of H-Ni/NiO/C is only slightly altered compared to the initial curve. In particular, the overvoltage at 10 mA cm<sup>-2</sup> is increased only by 5 mV after 2000 cycles. The constant potential results reveal that nearly 90% of the initial current density is maintained after 12 h of operation. In addition, the crystal phase and morphological structure of H-Ni/NiO/C were confirmed by XRD and SEM after stability testing (Additional file 1: Fig. S8). The result revealed that H-Ni/NiO/C exhibited outstanding durability in alkaline environments. The mechanism of the HER using the H-Ni/NiO/C electrocatalyst is shown in Fig. 6b. In this mechanism, when water molecules are absorbed at the Ni/NiO interface, NiO moieties drive H-OH bond breakage to create adsorbed hydrogen atoms ( $H_{ads}$ ) and hydroxyl ions ( $OH^-$ ), whereas Ni

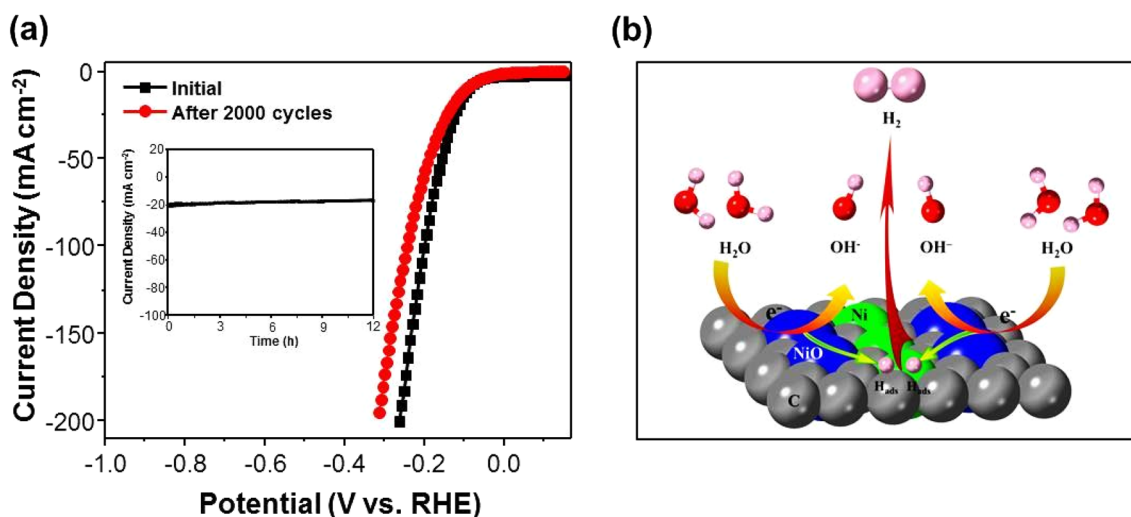


**Fig. 6** **a** Polarization curves recorded initially and after 2000 CV cycles of H-Ni/NiO/C. Inset: Current–time response of H-Ni/NiO/C obtained at  $-0.198$  V for 12 h. **b** Schematic of the proposed HER mechanism using the H-Ni/NiO/C catalyst

moieties recombine  $H_{ads}$  to produce  $H_2$ . This synergistic effect helps H-Ni/NiO/C achieve a higher HER activity than bare electrocatalysts.

#### 4 Conclusion

In conclusion, Ni/NiO/C hollow-structured composites were successfully fabricated from Ni-MOF precursors and utilized as efficient electrocatalysts for the HER in alkaline media. The experimental results confirmed that H-Ni/NiO/C exhibited better HER activity than H-Ni/C, H-NiO/C, and non-hollow NH-Ni/NiO/C catalysts. Notably, H-Ni/NiO/C exhibited a very low overvoltage of 87 mV at a current density of  $10 \text{ mA cm}^{-2}$ . In addition, this catalyst exhibited remarkable stability after 12 h test. The good HER activity was assigned to the emerging effect of the metal/metal oxide and hollow morphological structure, which facilitated H-OH bond breakage, the recombination of intermediate hydrogen, and electron transfer. The empirical findings of this study provide a novel understanding of the use of MOFs for the fabrication of economical catalysts for  $H_2$  production.

$C_2H_5OH$	Ethanol
DI	De-ionized
GCE	Glassy carbon electrode
LSV	Linear sweep voltammetry
RHE	Reference hydrogen electrode
ECSA	Electrochemical active surface area
$C_{dl}$	Double-layer capacitance

#### Supplementary Information

The online version contains supplementary material available at <https://doi.org/10.1186/s40580-023-00354-w>.

**Additional file 1: Figure S1.** (a) XRD pattern and (b) FE-SEM image of the Ni-MOF hollow structure. **Figure S2.** SEM images of (a) H-Ni/C and (b) H-NiO/C. **Figure S3.** (a) TEM, and (b) Field emission TEM images of H-Ni/C. **Figure S4.** (a) XPS survey spectrum. High-resolution XPS profiles of H-NiO/C: (b) Ni 2p, (c) O 1s, and (d) C 1s. **Figure S5.** High-resolution XPS profiles of H-Ni/C: (a) Ni 2p, and (b) C 1s. **Figure S6.** (a) Polarization curves of the H-Ni/NiO/C-10min, H-Ni/NiO/C-20min, and H-Ni/NiO/C-30min catalysts at a scan rate of  $2 \text{ mV s}^{-1}$  in a 1 M KOH solution. (b) Tafel plots of the same catalysts derived from (a). **Figure S7.** Cyclic voltammograms ( $0.1\text{--}0.2$  V) of (a) H-Ni/C, (b) H-Ni/NiO/C, (c) H-NiO/C, and (d) NH-Ni/NiO/C at various scan rates ( $20\text{--}120 \text{ mV s}^{-1}$ ) in a 1 M KOH solution. **Figure S8.** (a) XRD pattern and (b) SEM images of H-Ni/NiO/C after 2000 CV cycles. **Table S1.** Comparison of the HER performance of different samples in an alkaline solution. **Table S2.** Comparison of the catalytic activity of the Ni/NiO/C hollow structure with those of nickel-based catalysts for the HER in an alkaline solution.

#### Abbreviations

$H_2$	Hydrogen
HER	Hydrogen evolution reaction
TM	Transition metal
TMO	Transition metal oxide
MOFs	Metal-organic framework
SEM	Scanning electron microscopy
XRD	X-ray diffraction
XPS	X-ray photoelectron spectroscopy
CV	Cyclic voltammetry
EIS	Electrochemical impedance spectroscopy
TEM	Transmission electron microscopy
HR-TEM	High resolution-transmission electron microscopy
PVP	Polyvinylpyrrolidone

#### Author contributions

HHD: methodology, investigation, data curation, writing-original draft. MAT: methodology. QVL: methodology. JHC: methodology. SHA: methodology, supervision. SYK: methodology, supervision, writing review and editing, project administration. All authors read and approved the final manuscript.

#### Funding

This research was supported in part by the National Research Foundation of Korea (NRF) (NRF-2021R1A4A3027878) and the "Creative Materials Discovery Program" (NRF-2017M3D1A1039379). This research was also supported by the Brain Pool Program through the National Research Foundation of Korea (NRF), funded by the Ministry of Science and ICT (Grant number 2020H1D3A1A04081409).



**Availability of data and materials**

The datasets used and/or analyzed during the current study are available from the corresponding author upon reasonable request.

**Declarations****Competing interests**

The authors declare that they have no competing interests.

Received: 22 September 2022 Accepted: 6 January 2023

Published online: 02 February 2023

**References**

1. X. Wang, J. He, B. Yu, B. Sun, D. Yang, X. Zhang, Q. Zhang, W. Zhang, L. Gu, Y. Chen, CoSe<sub>2</sub> nanoparticles embedded MOF-derived Co-NC nanoflake arrays as efficient and stable electrocatalyst for hydrogen evolution reaction. *Appl. Catal. B* **258**, 117996 (2019)
2. Y. Wang, F. Lu, K. Su, N. Zhang, Y. Zhang, M. Wang, X. Wang, Engineering Mo-O-C interface in MoS<sub>2</sub>@rGO via charge transfer boosts hydrogen evolution. *Chem. Eng. J.* **399**, 126018 (2020)
3. S.A. Shah, L. Xu, R. Sayyar, T. Bian, Z. Liu, A. Yuan, X. Shen, I. Khan, A.A. Tahir, H. Ullah, Growth of MoS<sub>2</sub> nanosheets on M@N-doped carbon particles (M= Co, Fe or CoFe Alloy) as an efficient electrocatalyst toward hydrogen evolution reaction. *Chem. Eng. J.* **428**, 132126 (2022)
4. V.-H. Nguyen, H.H. Do, T. Van Nguyen, P. Singh, P. Raizada, A. Sharma, S.S. Sana, A.N. Grace, M. Shokouhimehr, S.H. Ahn, Perovskite oxide-based photocatalysts for solar-driven hydrogen production: progress and perspectives. *Sol. Energy* **211**, 584–599 (2020)
5. H.H. Do, D.L.T. Nguyen, X.C. Nguyen, T.-H. Le, T.P. Nguyen, Q.T. Trinh, S.H. Ahn, D.-V.N. Vo, S.Y. Kim, Q. Van Le, Recent progress in TiO<sub>2</sub>-based photocatalysts for hydrogen evolution reaction: a review. *Arab. J. Chem.* **13**, 3653–3671 (2020)
6. F. Davodi, G. Cilpa-Karhu, J. Sainio, M. Tavakkoli, H. Jiang, E. Mühlhausen, G. Marzun, B. Gökce, K. Laasonen, T. Kallio, Designing of low Pt electrocatalyst through immobilization on metal@C support for efficient hydrogen evolution reaction in acidic media. *J. Electroanal. Chem.* **896**, 115076 (2021)
7. A. Shan, X. Teng, Y. Zhang, P. Zhang, Y. Xu, C. Liu, H. Li, H. Ye, R. Wang, Interfacial electronic structure modulation of Pt-MoS<sub>2</sub> heterostructure for enhancing electrocatalytic hydrogen evolution reaction. *Nano Energy* **94**, 106913 (2022)
8. J. Zhu, Y. Tu, L. Cai, H. Ma, Y. Chai, L. Zhang, W. Zhang, Defect-assisted anchoring of Pt single atoms on MoS<sub>2</sub> nanosheets produces high-performance catalyst for industrial hydrogen evolution reaction. *Small* **18**, 2104824 (2021)
9. H.H. Do, Q.V. Le, T.H. Lee, S.H. Hong, S.H. Ahn, H.W. Jang, S.Y. Kim, Core-shell architecture of NiSe<sub>2</sub> nanoparticles@nitrogen-doped carbon for hydrogen evolution reaction in acidic and alkaline media. *Int. J. Energy Res.* **45**, 20463–20473 (2021)
10. X. Fang, Z. Wang, Z. Jiang, J. Wang, M. Dong, Coral-like S-doped CoSe<sub>2</sub> with enriched 1T-phase as efficient electrocatalyst for hydrogen evolution reaction. *Electrochim. Acta* **322**, 134739 (2019)
11. C. Liu, Y. Hu, F. Liu, H. Liu, X. Xu, Y. Xue, J. Zhang, Y. Li, C. Tang, Electronic structure modulation of CoSe<sub>2</sub> nanowire arrays by tin doping toward efficient hydrogen evolution. *Int. J. Hydrog. Energy* **46**, 17133–17142 (2021)
12. L. Zhu, B. Yang, Z. Wu, C. Li, H. Li, H. Li, Y. Huang, X. Zhu, X. Zhu, Y. Sun, Metal/antiperovskite metal nitride composites Ag/AgNNi<sub>3</sub> as novel efficient electrocatalysts for hydrogen evolution reaction in alkaline media. *J. Mater. Sci. Technol.* **112**, 222–229 (2022)
13. W. Liu, T. Xia, Y. Ye, H. Wang, Z. Fang, Z. Du, X. Hou, Self-supported Ni<sub>3</sub>N nanoarray as an efficient nonnoble-metal catalyst for alkaline hydrogen evolution reaction. *Int. J. Hydrog. Energy* **46**, 27037–27043 (2021)
14. W. Hua, H. Sun, H. Liu, Y. Li, J.-G. Wang, Interface engineered NiMoN/Ni<sub>3</sub>N heterostructures for enhanced alkaline hydrogen evolution reaction. *Appl. Surf. Sci.* **540**, 148407 (2021)
15. D. Reynard, B. Nagar, H. Girault, Photonic flash synthesis of Mo<sub>2</sub>C/graphene electrocatalyst for the hydrogen evolution reaction. *ACS Catal.* **11**, 5865–5872 (2021)
16. W. Liu, X. Wang, F. Wang, K. Du, Z. Zhang, Y. Guo, H. Yin, D. Wang, A durable and pH-universal self-standing MoC–Mo<sub>2</sub>C heterojunction electrode for efficient hydrogen evolution reaction. *Nat. Commun.* **12**, 1–10 (2021)
17. Y. Li, X. Wu, H. Zhang, J. Zhang, Interface designing over WS<sub>2</sub>/W<sub>2</sub>C for enhanced hydrogen evolution catalysis. *ACS Appl. Energy Mater.* **1**, 3377–3384 (2018)
18. T.P. Nguyen, S.Y. Kim, T.H. Lee, H.W. Jang, Q. Van Le, I.T. Kim, Facile synthesis of W<sub>2</sub>C@WS<sub>2</sub> alloy nanoflowers and their hydrogen generation performance. *Appl. Surf. Sci.* **504**, 144389 (2020)
19. G.-H. Lee, Catalyst-free thermal evaporation synthesis of TiO<sub>2</sub> nanostructures in atmospheric air. *Korean J. Met. Mater.* **58**, 353–356 (2020)
20. M.J. Kim, S.-H. Bak, J. Hahn, S.J. Kim, D.B. Lee, High-temperature oxidation of Fe-12Cr-0.3C-4Mn-(13–15)Cu composite ALLOYS. *Korean J. Met. Mater.* **57**, 575–581 (2019)
21. H.H. Do, Q. Van Le, M.A. Tekalgne, A.V. Tran, T.H. Lee, S.H. Hong, S.M. Han, S.H. Ahn, Y.J. Kim, H.W. Jang, Metal-organic framework-derived MoS<sub>x</sub> composites as efficient electrocatalysts for hydrogen evolution reaction. *J. Alloys Compd.* **852**, 156952 (2021)
22. H.H. Do, Q.V. Le, T.V. Nguyen, K.A. Huynh, M.A. Tekalgne, V.A. Tran, T.H. Lee, J.H. Cho, M. Shokouhimehr, S.H. Ahn, Synthesis of MoS<sub>x</sub>/Ni-metal-organic framework-74 composites as efficient electrocatalysts for hydrogen evolution reactions. *Int. J. Energy Res.* **45**, 9638–9647 (2021)
23. J.K. Nørskov, T. Bligaard, A. Logadottir, J. Kitchin, J.G. Chen, S. Pandalov, U. Stimming, Trends in the exchange current for hydrogen evolution. *J. Electrochem. Soc.* **152**, J23 (2005)
24. L. Yu, Q. Zhu, S. Song, B. McElhenny, D. Wang, C. Wu, Z. Qin, J. Bao, Y. Yu, S. Chen, Non-noble metal-nitride based electrocatalysts for high-performance alkaline seawater electrolysis. *Nat. Commun.* **10**, 1–10 (2019)
25. Y.F. Xu, M.R. Gao, Y.R. Zheng, J. Jiang, S.H. Yu, Nickel/nickel (II) oxide nanoparticles anchored onto cobalt (IV) diselenide nanobelts for the electrochemical production of hydrogen. *Angew. Chem.* **125**, 8708–8712 (2013)
26. A.G. Oshchepkov, A. Bonnefont, V.A. Saveleva, V. Papaefthimiou, S. Zafeirotos, S.N. Pronkin, V.N. Parmon, E.R. Savinova, Exploring the influence of the nickel oxide species on the kinetics of hydrogen electrode reactions in alkaline media. *Top. Catal.* **59**, 1319–1331 (2016)
27. X. Yan, L. Tian, X. Chen, Crystalline/amorphous Ni/NiO core/shell nanosheets as highly active electrocatalysts for hydrogen evolution reaction. *J. Power Sources* **300**, 336–343 (2015)
28. J. Wang, S. Mao, Z. Liu, Z. Wei, H. Wang, Y. Chen, Y. Wang, Dominating role of Ni<sup>0</sup> on the interface of Ni/NiO for enhanced hydrogen evolution reaction. *ACS Appl. Mater. Interfaces* **9**, 7139–7147 (2017)
29. L. Yang, X. Zhao, R. Yang, P. Zhao, Y. Li, P. Yang, J. Wang, D. Astruc, In-situ growth of carbon nanotubes on Ni/NiO nanofibers as efficient hydrogen evolution reaction catalysts in alkaline media. *Appl. Surf. Sci.* **491**, 294–300 (2019)
30. H. Han, S. Park, D. Jang, W.B. Kim, N-doped carbon nanoweb-supported Ni/NiO heterostructure as hybrid catalysts for hydrogen evolution reaction in an alkaline phase. *J. Alloys Compd.* **853**, 157338 (2021)
31. M. Gong, W. Zhou, M.-C. Tsai, J. Zhou, M. Guan, M.-C. Lin, B. Zhang, Y. Hu, D.-Y. Wang, J. Yang, Nanoscale nickel oxide/nickel heterostructures for active hydrogen evolution electrocatalysis. *Nat. Commun.* **5**, 1–6 (2014)
32. X. Yan, L. Tian, M. He, X. Chen, Three-dimensional crystalline/amorphous Co/Co<sub>3</sub>O<sub>4</sub> core/shell nanosheets as efficient electrocatalysts for the hydrogen evolution reaction. *Nano Lett.* **15**, 6015–6021 (2015)
33. C. Bai, S. Wei, D. Deng, X. Lin, M. Zheng, Q. Dong, A nitrogen-doped nano carbon dodecahedron with Co@Co<sub>3</sub>O<sub>4</sub> implants as a bi-functional electrocatalyst for efficient overall water splitting. *J. Mater. Chem. A* **5**, 9533–9536 (2017)
34. H. Jin, J. Wang, D. Su, Z. Wei, Z. Pang, Y. Wang, In situ cobalt–cobalt oxide/N-doped carbon hybrids as superior bifunctional electrocatalysts for hydrogen and oxygen evolution. *J. Am. Chem. Soc.* **137**, 2688–2694 (2015)
35. S. Wang, Y. Wang, S.Q. Zang, X.W. Lou, Hierarchical hollow heterostructures for photocatalytic CO<sub>2</sub> reduction and water splitting. *Small Methods* **4**, 1900586 (2020)
36. Y. Wang, S. Wang, X.W. Lou, Dispersed nickel cobalt oxyphosphide nanoparticles confined in multichannel hollow carbon fibers for

- photocatalytic CO<sub>2</sub> reduction. *Angew. Chem. Int. Ed.* **58**, 17236–17240 (2019)
37. Y. Guo, J. Tang, H. Qian, Z. Wang, Y. Yamauchi, One-pot synthesis of zeolitic imidazolate framework 67-derived hollow Co<sub>3</sub>S<sub>4</sub>@MoS<sub>2</sub> heterostructures as efficient bifunctional catalysts. *Chem. Mater.* **29**, 5566–5573 (2017)
  38. M. Yang, C.H. Zhang, N.W. Li, D. Luan, L. Yu, X.W. Lou, Design and synthesis of hollow nanostructures for electrochemical water splitting. *Adv. Sci.* **9**, 2105135 (2022)
  39. Z.X. Cai, Z.L. Wang, J. Kim, Y. Yamauchi, Hollow functional materials derived from Metal-organic frameworks: synthetic strategies, conversion mechanisms, and electrochemical applications. *Adv. Mater.* **31**, 1804903 (2019)
  40. T.P. Nguyen, D.L.T. Nguyen, V.-H. Nguyen, T.-H. Le, Q.V. Ly, D.-V.N. Vo, Q.V. Nguyen, H.S. Le, H.W. Jang, S.Y. Kim, Facile synthesis of WS<sub>2</sub> hollow spheres and their hydrogen evolution reaction performance. *Appl. Surf. Sci.* **505**, 144574 (2020)
  41. V. Ganesan, J. Kim, Multi-shelled CoS<sub>2</sub>–MoS<sub>2</sub> hollow spheres as efficient bifunctional electrocatalysts for overall water splitting. *Int. J. Hydrog. Energy* **45**, 13290–13299 (2020)
  42. T. Xia, L. Zhou, S. Gu, H. Gao, X. Ren, S. Li, R. Wang, H. Guo, A subtle functional design of hollow CoP@MoS<sub>2</sub> hetero-nanoframes with excellent hydrogen evolution performance. *Mater. Des.* **211**, 110165 (2021)
  43. Y. Xue, X. Wang, M. Zhu, Q. Yan, K. Zhu, K. Cheng, K. Ye, J. Yan, D. Cao, G. Wang, Construction of hollow structure cobalt iron selenide polyhedrons for efficient hydrogen evolution reaction. *Int. J. Energy Res.* **44**, 12045–12055 (2020)
  44. T. Tian, L. Huang, L. Ai, J. Jiang, Surface anion-rich NiS<sub>2</sub> hollow microspheres derived from Metal-organic frameworks as a robust electrocatalyst for the hydrogen evolution reaction. *J. Mater. Chem. A* **5**, 20985–20992 (2017)
  45. F. Zou, Y.-M. Chen, K. Liu, Z. Yu, W. Liang, S.M. Bhaway, M. Gao, Y. Zhu, Metal organic frameworks derived hierarchical hollow NiO/Ni/graphene composites for lithium and sodium storage. *ACS Nano* **10**, 377–386 (2016)
  46. Z. Lv, X. Tan, C. Wang, A. Alsaedi, T. Hayat, C. Chen, Metal-organic frameworks-derived 3D yolk shell-like structure Ni@carbon as a recyclable catalyst for Cr(VI) reduction. *Chem. Eng. J.* **389**, 123428 (2020)
  47. X. Wang, Q. Geng, G. Shi, Y. Zhang, D. Li, MOF-derived yolk-shell Ni/C architectures assembled with Ni@C core-shell nanoparticles for lightweight microwave absorbents. *CrystEngComm* **22**, 6796–6804 (2020)
  48. Y. Qiu, Y. Lin, H. Yang, L. Wang, M. Wang, B. Wen, Hollow Ni/C microspheres derived from Ni-metal organic framework for electromagnetic wave absorption. *Chem. Eng. J.* **383**, 123207 (2020)
  49. W. Liu, Q. Shao, G. Ji, X. Liang, Y. Cheng, B. Quan, Y. Du, Metal-organic-frameworks derived porous carbon-wrapped Ni composites with optimized impedance matching as excellent lightweight electromagnetic wave absorber. *Chem. Eng. J.* **313**, 734–744 (2017)
  50. H. Yan, D. Zhang, J. Xu, Y. Lu, Y. Liu, K. Qiu, Y. Zhang, Y. Luo, Solution growth of NiO nanosheets supported on Ni foam as high-performance electrodes for supercapacitors. *Nanoscale Res. Lett.* **9**, 1–7 (2014)
  51. J. Wang, Z. Zhao, C. Shen, H. Liu, X. Pang, M. Gao, J. Mu, F. Cao, G. Li, Ni/NiO heterostructures encapsulated in oxygen-doped graphene as multi-functional electrocatalysts for the HER, UOR and HMF oxidation reaction. *Catal. Sci. Technol.* **11**, 2480–2490 (2021)
  52. A.Y. Faid, A.O. Barnett, F. Seland, S. Sunde, Ni/NiO nanosheets for alkaline hydrogen evolution reaction: In situ electrochemical-Raman study. *Electrochim. Acta* **361**, 137040 (2020)
  53. P. Salunkhe, A.V. Muhammed Ali, D. Kekuda, Investigation on tailoring physical properties of Nickel Oxide thin films grown by dc magnetron sputtering. *Mater. Res. Express* **7**, 016427 (2020)
  54. W. Huang, S. Ding, Y. Chen, W. Hao, X. Lai, J. Peng, J. Tu, Y. Cao, X. Li, 3D NiO hollow sphere/reduced graphene oxide composite for high-performance glucose biosensor. *Sci. Rep.* **7**, 1–11 (2017)
  55. Z. Chen, T. Dedova, I.O. Acik, M. Danilson, M. Krunks, Nickel oxide films by chemical spray: Effect of deposition temperature and solvent type on structural, optical, and surface properties. *Appl. Surf. Sci.* **548**, 149118 (2021)
  56. N. Mironova-Ulmane, A. Kuzmin, I. Sildos, L. Puust, J. Grabis, Magnon and phonon excitations in nanosized NiO. *Latv. J. Phys. Tech. Sci.* **56**, 61–72 (2019)
  57. M. Mishra, S. Barthwal, B.R. Tak, R. Singh, Temperature-driven perturbations in growth kinetics, structural and optical properties of NiO thin films. *Phys. Status Solidi A* **218**, 2100241 (2021)
  58. Y. Yang, Y. Huang, S. Zhou, Y. Liu, L. Shi, T.T. Isimjan, X. Yang, Delicate surface vacancies engineering of Ru doped MOF-derived Ni-NiO@C hollow microsphere superstructure to achieve outstanding hydrogen oxidation performance. *J. Energy Chem.* **72**, 395–404 (2022)
  59. A. Sunny, K. Balasubramanian, Raman spectral probe on size-dependent surface optical phonon modes and magnon properties of NiO nanoparticles. *J. Phys. Chem. C* **124**, 12636–12644 (2020)
  60. N. Srinivasa, J.P. Hughes, P.S. Adarakatti, C. Manjunatha, S.J. Rowley-Neale, S. Ashoka, C.E. Banks, Facile synthesis of Ni/NiO nanocomposites: the effect of Ni content in NiO upon the oxygen evolution reaction within alkaline media. *RSC Adv.* **11**, 14654–14664 (2021)
  61. J. Jiang, R. Sun, X. Huang, H. Cong, J. Tang, W. Xu, M. Li, Y. Chen, Y. Wang, S. Han, CoS<sub>2</sub> quantum dots modified by ZIF-67 and anchored on reduced graphene oxide as an efficient catalyst for hydrogen evolution reaction. *Chem. Eng. J.* **430**, 132634 (2022)
  62. P.A. Thiel, T.E. Madey, The interaction of water with solid surfaces: fundamental aspects. *Surf. Sci. Rep.* **7**, 211–385 (1987)
  63. J. Greeley, T.F. Jaramillo, J. Bonde, I. Chorkendorff, J.K. Nørskov, Computational high-throughput screening of electrocatalytic materials for hydrogen evolution. *Nat. Mater.* **5**, 909–913 (2006)
  64. M. Gong, D.-Y. Wang, C.-C. Chen, B.-J. Hwang, H. Dai, A mini review on nickel-based electrocatalysts for alkaline hydrogen evolution reaction. *Nano Res.* **9**, 28–46 (2016)
  65. R. Zhang, R. Zhu, Y. Li, Z. Hui, Y. Song, Y. Cheng, J. Lu, CoP and Ni<sub>2</sub>P implanted in a hollow porous N-doped carbon polyhedron for pH universal hydrogen evolution reaction and alkaline overall water splitting. *Nanoscale* **12**, 23851–23858 (2020)
  66. Z. Li, D. Wu, Y. Ouyang, H. Wu, M. Jiang, F. Wang, L.Y. Zhang, Synthesis of hollow cobalt phosphide nanocrystals with ultrathin shells anchored on reduced graphene oxide as an electrocatalyst toward hydrogen evolution. *Appl. Surf. Sci.* **506**, 144975 (2020)

## Publisher's Note

Springer Nature remains neutral with regard to jurisdictional claims in published maps and institutional affiliations.

Submit your manuscript to a SpringerOpen® journal and benefit from:

- Convenient online submission
- Rigorous peer review
- Open access: articles freely available online
- High visibility within the field
- Retaining the copyright to your article

Submit your next manuscript at ► [springeropen.com](https://www.springeropen.com)